



A01-16874

AIAA 2001-1092

Dynamics of Swirling Premixed and Spray Flames

S. Menon, V. Sankaran, C. Stone,
*School of Aerospace Engineering
Georgia Institute of Technology
Atlanta, Georgia 30332*

and

B. Sekar
*Wright Patterson AFB
Dayton, Ohio 45433*

**39th AIAA Aerospace Sciences Meeting and
Exhibit
January 8-11, 2001 / Reno, NV**

Dynamics of Swirling Premixed and Spray Flames

S. Menon*, V. Sankaran†, C. Stone‡

*School of Aerospace Engineering
Georgia Institute of Technology
Atlanta, Georgia 30332*

and

B. Sekar§

*Wright Patterson AFB
Dayton, Ohio 45433*

This paper focuses on the general Large-Eddy Simulations (LES) formulation to simulate premixed and non-premixed combustion in complex flows such as those typically encountered in gas-turbine combustors. This formulation allows the study and analysis of the fundamental physics involved in such flows, i.e., vortex/flame interaction, combustion dynamics and stability, fuel-air mixing, droplet vaporization, and other aspects of combustion. A highly optimized, parallel LES solver capable of simulating a broad class of flows of practical interest in rather complex geometries has been developed. Typical flows studied include premixed flames in flamelet and broadened flamelet regimes and non-premixed flames in single and two phase flows. Current progress in model development and applications is presented.

1 Introduction

The simulation of compressible, swirling, turbulent reacting flows such as those found in contemporary power generation systems pose a great challenge due to the widely varying time and length scales. In addition to turbulence closure difficulties, the presence of multiple modes/regimes of combustion and the interaction between various chemical species and physical phases (liquid and gas) in the same combustion device accentuates the difficulties. Even with the current computational power available, Direct Numerical Simulation (DNS) of practical combustion devices is not possible. However, recently developed Large-Eddy Simulations (LES) methodologies may allow the accurate simulation of such complex environments at a reasonable computational expense.

In LES, only turbulent flow scales larger than a cut-off size are computed using a time and space accurate scheme while the effects of the smaller, unresolved scales (assumed to be mostly isotropic) are modeled, generally by employing eddy viscosity-based sub-grid models. This approach is acceptable for momentum transport since most of the energy containing scales are resolved. However, this argument cannot readily be extended to reacting flows since combustion occurs at the molecular level, far below any resolved scale.

Accurate modeling of scalar mixing (fuel and oxidizer) is critical for a realistic prediction of chemical reaction rates. Since, the scalar mixing process is dominated by small, turbulent scales, *ad hoc* eddy diffusivity concepts cannot be accurately used. To deal with these distinctly different modeling requirements, a new sub-grid mixing and combustion model has been developed that allows for proper resolution of the small-scale scalar mixing and combustion effects within the framework of a conventional LES approach.

Earlier studies¹⁻³ have established the ability of the LES model in premixed combustion and in fuel-air mixing. To reduce the computational cost, the past calculations employed flamelet models (for premixed combustion) or simulated fuel-air mixing without detailed chemical kinetics. Earlier studies on two-phase reacting flows by Pannala and Menon⁴ involves the use of a zero Mach number formulation of Navier-Stokes equation to predict mixing and combustion in spray flames. This paper summarizes the effort in developing a parallel, LES solver to study combustion dynamics (fully premixed combustion) and spray combustion in a realistic gas turbine configuration.

2 Large-Eddy Simulation Model

The governing conservation equations of motion for mass, momentum, energy, and species in a compress-

*Professor, AIAA Senior Member

†Graduate Research Assistant, AIAA Student Member

‡Graduate Research Assistant, AIAA Student Member

§AIAA Member

Copyright © 2001 by Menon, Stone and Sankaran. Published by the American Institute of Aeronautics and Astronautics, Inc. with permission.

ible, reacting flow are:

$$\begin{aligned} \frac{\partial \rho}{\partial t} + \frac{\partial \rho u_i}{\partial x_i} &= 0 \\ \frac{\partial \rho u_i}{\partial t} + \frac{\partial}{\partial x_j} [\rho u_i u_j + p \delta_{ij} - \tau_{ij}] &= 0 \\ \frac{\partial \rho E}{\partial t} + \frac{\partial}{\partial x_i} [(\rho E + p) u_i + q_i - u_j \tau_{ji}] &= 0 \\ \frac{\partial \rho Y_m}{\partial t} + \frac{\partial}{\partial x_i} [\rho Y_m (u_i + V_{i,m})] &= \dot{w}_m \quad m = 1, N \end{aligned} \quad (1)$$

Here, ρ is the mass density, p is the pressure, E is the total energy per unit mass, u_i is the velocity vector, q_i is the heat flux vector, τ_{ij} is the viscous stress tensor, and N is the total number of chemical species. The individual species mass fraction, diffusion velocities, and mass reaction rate per unit volume are, respectively, Y_m , $V_{i,m}$, and \dot{w}_m . The viscous stress tensor is $\tau_{ij} = \mu(\partial u_i / \partial x_j + \partial u_j / \partial x_i) - \frac{2}{3} \mu (\partial u_k / \partial x_k) \delta_{ij}$ where μ is the molecular viscosity coefficient approximated using Sutherland's law. The diffusion velocities are approximated by Fick's law: $V_{i,m} = (-D_m / Y_m) (\partial Y_m / \partial x_i)$ where D_m is the m -th species mixture averaged molecular diffusion coefficient. The pressure is determined from the equation of state for a perfect gas mixture

$$P = \rho T \sum_{m=1}^N Y_m R_u / W_m \quad (2)$$

where T is the temperature, R_u is the universal gas constant, and W_m the species molecular weight. The total energy per unit volume is determined from $\rho E = \rho(e + \frac{1}{2} u_k^2)$ where e is the internal energy per unit mass given by $e = \sum_{m=1}^N Y_m h_m - P / \rho$ and h_m is the species enthalpy. Finally, the caloric equation of state is given by

$$h_m = \Delta h_{f,m}^0 + \int_{T^0}^T c_{p,m}(T) dT \quad (3)$$

where $\Delta h_{f,m}^0$ is the standard heat of formation at temperature T^0 and $c_{p,m}$ is the m -th species specific heat at constant pressure.

Following Erlebacher *et al.*,⁵ the flow variables can be decomposed into the super-grid (i.e., resolved) and sub-grid (i.e., unresolved) components by a spatial filtering operation such that $f = \bar{f} + f''$ where $\bar{\sim}$ and $''$ denote resolved super-grid and unresolved fluctuating sub-grid quantities, respectively. The resolved super-grid quantities are determined by Favre filtering:

$$\bar{f} = \frac{\rho \tilde{f}}{\bar{\rho}} \quad (4)$$

where the over-bar represents spatial filtering defined as

$$\bar{f}(x_i, t) = \int f(x'_i, t) G_f(x_i, x'_i) dx'_i. \quad (5)$$

Here, G_f is the filter kernel and the integral is over the entire domain. Applying the filtering operation (a low-pass filter of grid size $\bar{\Delta}$) to the Navier-Stokes

equations, the following LES equations are obtained:

$$\begin{aligned} \frac{\partial \bar{\rho}}{\partial t} + \frac{\partial \bar{\rho} \tilde{u}_i}{\partial x_i} &= 0 \\ \frac{\partial \bar{\rho} \tilde{u}_i}{\partial t} + \frac{\partial}{\partial x_j} [\bar{\rho} \tilde{u}_i \tilde{u}_j + \bar{p} \delta_{ij} - \bar{\tau}_{ij} + \tau_{ij}^{sgs}] &= 0 \\ \frac{\partial \bar{\rho} \tilde{E}}{\partial t} + \frac{\partial}{\partial x_i} [(\bar{\rho} \tilde{E} + \bar{p}) \tilde{u}_i + \bar{q}_i - \tilde{u}_j \bar{\tau}_{ji} + H_i^{sgs} + \sigma_{ij}^{sgs}] &= 0 \\ \frac{\partial \bar{\rho} \tilde{Y}_m}{\partial t} + \frac{\partial}{\partial x_i} [\bar{\rho} \tilde{Y}_m \tilde{u}_i - \bar{\rho} \tilde{D}_m \frac{\partial \tilde{Y}_m}{\partial x_i} + \Phi_{i,m}^{sgs} + \theta_{i,m}^{sgs}] &= \bar{w}_m \end{aligned} \quad (6)$$

Here, $\bar{\tau}_{ij}$ and \bar{q}_i are approximated in terms of the filtered velocity. The pressure is determined from the filtered equation of state,

$$\bar{P} = \bar{\rho} R_u \sum_{k=1}^n \{ \tilde{Y}_k \bar{T} / W_k + [\tilde{Y}_k \bar{T} - \tilde{Y}_k \bar{T}] / W_k \} \quad (7)$$

which reduces to

$$\bar{P} = \bar{\rho} R \bar{T} \quad (8)$$

when the second order correlation terms are neglected.

The unclosed sub-grid terms representing respectively, the sub-grid stress tensor, sub-grid heat flux, unresolved viscous work, species mass flux, diffusive mass flux, and filtered reaction rate are:

$$\begin{aligned} \tau_{ij}^{sgs} &= \bar{\rho} [\tilde{u}_i \tilde{u}_j - \tilde{u}_i \tilde{u}_j] \\ H_i^{sgs} &= \bar{\rho} [\tilde{E} \tilde{u}_i - \tilde{E} \tilde{u}_i] + [\bar{p} \tilde{u}_i - \bar{p} \tilde{u}_i] \\ \sigma_i^{sgs} &= [\tilde{u}_j \bar{\tau}_{ij} - \tilde{u}_j \bar{\tau}_{ij}] \\ \Phi_{i,m}^{sgs} &= \bar{\rho} [\tilde{u}_i \tilde{Y}_m - \tilde{u}_i \tilde{Y}_m] \\ \theta_{i,m}^{sgs} &= \bar{\rho} [V_{i,m} \tilde{Y}_m - \tilde{V}_{i,m} \tilde{Y}_m] \\ \bar{w}_m & \end{aligned} \quad (9)$$

2.1 k^{sgs} Sub-grid Closure

In the present approach, the sub-grid stress tensor, $\tau_{i,j}^{sgs}$, is determined by using the local grid size, $\bar{\Delta}$, as the characteristic length scale and the sub-grid kinetic energy, k^{sgs} , as the characteristic velocity scale. Therefore, a transport equation for k^{sgs} is solved in addition to the governing mass, momentum, and energy conservation equations 6.

The sub-grid kinetic energy, $k^{sgs} = \frac{1}{2} [\tilde{u}_k^2 - \bar{u}_k^2]$ is obtained by solving the following transport equation:⁶

$$\frac{\partial \bar{\rho} k^{sgs}}{\partial t} + \frac{\partial}{\partial x_i} (\bar{\rho} \tilde{u}_i k^{sgs}) = P^{sgs} - D^{sgs} + \frac{\partial}{\partial x_i} \left(\frac{\nu_t}{Pr_t} \frac{\partial k^{sgs}}{\partial x_i} \right) \quad (10)$$

where Pr_t is the turbulent Prandtl number (taken as constant and equal to 0.90), P^{sgs} and D^{sgs} are, respectively, the production and dissipation of sub-grid kinetic energy. The production term is defined as, $P^{sgs} = -\tau_{ij}^{sgs} (\partial \tilde{u}_i / \partial x_j)$, where τ_{ij}^{sgs} is the modeled sub-grid stress tensor. τ_{ij}^{sgs} is modeled as

$$\tau_{ij}^{sgs} = -2\bar{\rho} \nu_t (\tilde{S}_{ij} - \frac{1}{3} \tilde{S}_{kk} \delta_{ij}) + \frac{2}{3} \bar{\rho} k^{sgs} \delta_{ij} \quad (11)$$

with the eddy viscosity, $\nu_t = C_\nu (k^{sgs})^{1/2} \bar{\Delta}$ where $\bar{\Delta}$ is the characteristic LES grid size and the resolved

rate-of-strain tensor, $\tilde{S}_{ij} = \frac{1}{2}(\partial\tilde{u}_i/\partial x_j + \partial\tilde{u}_j/\partial x_i)$. Finally, the dissipation term is modeled as $D^{sgs} = C_\varepsilon \bar{\rho} (k^{sgs})^{3/2} / \Delta$. The coefficients, C_ν and C_ε are can be taken as constant (conventional closure) or can be dynamically determined locally.⁷

A distinct advantage of this k^{sgs} approach is that it does not assume equilibrium between sub-grid kinetic energy production and dissipation (implicit in algebraic models) thus, helping to attribute a relaxation time associated with non-equilibrium in the sub-grid scales. In addition to this advantage is that the effects of sub-grid turbulence on flame structure and propagation in premixed combustion can be quantified in terms of the sub-grid kinetic energy.^{1,2,8}

2.2 Liquid phase Simulation Model

Past studies of multi-phase flows,¹² have used an Eulerian/Lagrangian approach to compute the gas phase and liquid phase respectively. In this method the liquid droplets are tracked with a Lagrangian approach to explicitly compute the mass, momentum, energy and species transfer between the continuum and dispersed phase. Usually due to resource constraints, only a limited range of droplets are computed. Droplets below a certain *ad-hoc* cut-off size is assumed to evaporate instantaneously and to become fully mixed with the gas phase. But since this is not a valid assumption, Pannala and Menon⁴ extended the gas phase sub-grid mixing model, based on the Linear-Eddy Model (LEM), to allow simulation of the final stages of droplet vaporization and mixing. Their study was restricted to zero-Mach number formulation of the conservation equations. Also, the heat release rates and hence, the vaporization rate allowed in those simulations were low. The present work aims to extend and improve upon the previous study⁴ to include all the complexities that were ignored in the previous study. Thus, the current study on two-phase flows solves a full compressible Navier-Stokes equation with a single step global chemistry with realistic heat release. It is also intended to study both infinite rate and finite rate effects. To begin, studies were performed using the conventional gradient diffusion type of closure for the scalars and work is underway to implement the sub-grid scalar mixing model based LEM of Menon *et al*⁹ to close the scalar equations at the sub-grid scale.

3 Parallel LES Algorithm

The LES equations of motion are solved on a three dimensional, boundary-conforming, finite-volume grid using MacCormack's explicit scheme.¹³ No-slip, adiabatic wall conditions are used with non-reflecting inflow/outflow boundary conditions following Poinot *et al*.¹⁵ Clustering is employed near walls and in shear layers to better resolve large scale fluctuations. To increase simulation turn-around time, the computational domain is evenly distributed in parallel

using the Message-Passing Interface (MPI) standard. An advantage of the explicit scheme used here is the ease of load balancing since every cell requires the same amount of work resulting in high parallel efficiency attainable.

A cylindrical dump combustor consisting of an inlet pipe expanding into the larger combustion zone is simulated. A rendering of the physical device is shown in Fig. 1; however, the centerline injection probe is not included (currently under way). The ratio of combustor diameter (D_c) to inlet diameter (D_0) is 3.2. The inlet pipe is included to simulate the region downstream of a swirling premixer (Fig. 1). Additionally, by including the inlet, natural flow instabilities are allowed to form upstream of the dump plane. A swirling velocity profile with a swirl number of 0.56 is imposed at the inlet boundary. At this high swirl number, the peak azimuthal velocity is 10% higher than the axial velocity. The mean inlet mass flow rate, temperature, and pressure are 0.435 Kilograms/second, 673 Kelvin, and 11.8 atmospheres, respectively. The Reynolds number based on inlet bulk velocity and inlet diameter is 330,000. An inflow turbulent field is generated by using a specified turbulence intensity (7%) on a randomly generated Gaussian field. To wash out the effects of the initial conditions (approximated using turbulent jet profiles) the simulations are allowed to run several flow-through-times before any data is collected for analysis.

To excite acoustic resonance and accelerate the exiting flow, a 60% convergence is placed at the outflow; however, the flow remains sub-sonic. It must be noted that this sub-sonic condition is not the perfect pressure boundary obtained had the outflow been choked. The simulation grid and geometry is shown in Fig. 1. The computational grid is $141 \times 65 \times 81$ (742,365 total grid cells).

For the non-premixed simulations (two-phase), the droplets are injected near the centerline of the inlet boundary. Particle displacements were integrated using fourth order Runge-Kutta method. Elastic collisions were assumed for particles contacting the walls. Properties of the gas phase are interpolated to the droplet locations using simple averaging of the nearest eight neighbor cells. A total of 150,000 droplets are tracked for the momentum coupled case and 120,000 droplets for the reacting case, to obtain good statistics. Particles of constant size (20 microns) were introduced from the start of the simulation of the Eulerian field, assuming that this will reduce the time required for the transient evolution of the field. Stokes number of the particles injected based on the radius of the combustor is 8.2. Cut-off size of the droplets used in the reacting case simulation is 5 microns.

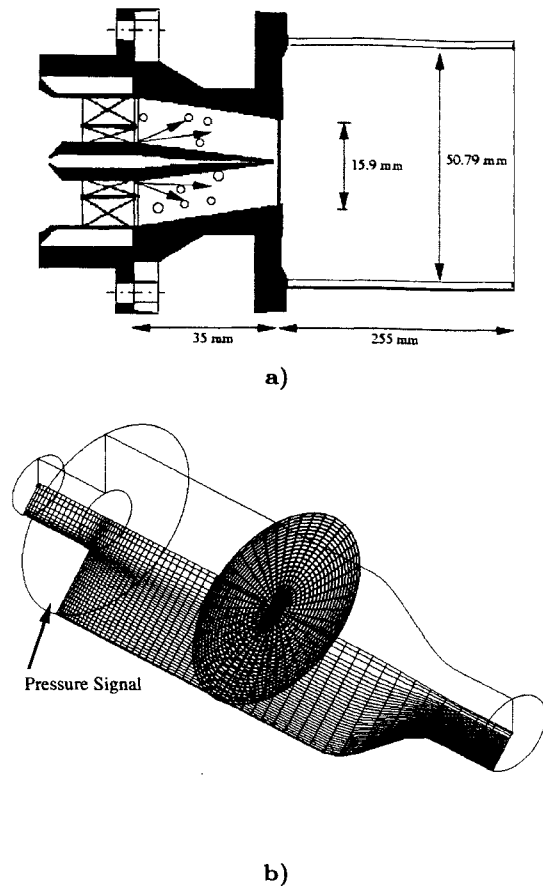


Fig. 1 Geometry (a) and computational grid (b) ($141 \times 65 \times 81$) employed in this study. Pressure signal is recorded at the base of the combustor.

4 LES of Combustion Dynamics

At the heart of combustion dynamics is the coupling between the heat release and the pressure oscillations in the combustor. Accurate prediction of the effects of such coupling is especially difficult due to the unsteadiness of the controlling processes (e.g., fuel injection) and the high nonlinearity of the interactions between turbulent mixing, acoustic wave motion, and unsteady heat release. Large-scale structures in the flow play a key role in the coupling process by controlling the mixing of the essential ingredients of combustion: oxidizer, fuel, and heat. Realizing this, attempts have been made to control the vorticity both passively and actively. Active control of instabilities through fuel modulation¹⁶ and flow control¹⁷ have been demonstrated in the past. Passive control using sudden expansions (dump combustor) or bluff-bodies have also been conducted but these studies predominately focused upon axisymmetric flow instability, characteristic of non-swirling flows. However, in a highly swirling flow, azimuthal (helical) instability modes are present and their effects may become important. Recently, experi-

mental and numerical studies have been conducted on highly swirling combustion flows.^{1,18}

Due to the increasing emission regulations, low- NO_x gas turbines (LNGT) employing lean, premixed combustion are in high demand. Lean, premixed combustion results in the reduction of thermal NO_x formation (Zeldovich or thermal NO_x mechanism) due to the reduction in flame temperature. However, lean operation is sensitive to small fluctuations in fuel concentration, flow velocity, temperature, and pressure. Under certain conditions, these fluctuations can be amplified, resulting in high-amplitude pressure oscillations. If these pressure pulses are not attenuated, they may lead to structural damage.

Swirl stabilized combustion is quite common in gas turbine combustors. However, it has been reported by Sivasegaram and Whitelaw¹⁹ that swirl may drive instability in sudden expansion flows. In order to control such swirl-enhanced instabilities, it is vital to understand the large-scale dynamics of these flows. In addition to the basic flow dynamics, the interaction of the vortex structures and the combustion processes needs to be studied.

4.1 Combustion Dynamics Simulation Model

Due to the high expense and numerical difficulties of finite-rate chemistry, the premixed combustion is modeled with a G -equation flamelet model.²⁰ In this model, a progress variable G is defined such that $G = 1$ for the non-reacted premixed gas and $G = 0$ for the burnt products. The evolution of the progress variable is balanced by the fluid convection and flame-normal burning rate. Details of the reaction rates and molecular diffusion/conduction are contained in the laminar flame speed, S_L . Once filtered, the G -equation requires a model for the turbulent flame speed, S_t . Recently, a *broadened flame model* for premixed combustion using dynamically evaluated turbulence quantities (Localized Dynamic K -equation Model, LDKM) has been developed by Kim and Menon.² This model allows the simulation of flames in the *thin-reaction-zones regime* over a wide range of turbulence levels. However, for this parametric study, Pocheau's flame speed model²¹ has been used in the following form;

$$\frac{S_t}{S_L} = \left(1 + \beta \frac{u'^\alpha}{S_L^\alpha}\right)^{\frac{1}{2}}. \quad (12)$$

Here, u' is the unresolved SGS velocity fluctuation, $\alpha = 2$ for energy conservation, and β is an adjustable parameter set to 20.¹

For this study in combustion dynamics, three simulations were conducted in order to observe the effects of swirl and heat release on the dynamics in this combustor. A non-swirling, non-reacting case (Case A) and two swirling, reacting cases, without (Case B) and with (Case C) heat release, will be compared. The product temperature of the heat release simulation

was 1807 Kelvin. No combustion was simulated for the non-swirling case since, at the specified inlet mass flow rate, the flame can not be held by the sudden expansion at the dump plane alone. In the limit of zero heat release, the flamelet (G -equation) field does not effect the flow and therefore acts as a passive scalar. In this limiting situation, the flamelet surface simply follows the local velocity-field without altering it through thermal expansion. While the absence of heat release is not physical, this type of simulation isolates the effects of turbulence and flow dynamics on the flame front.

4.2 Combustion Dynamics Results

The mean axial, radial, and tangential velocity profiles across the diameter of the combustor at the center plane for all three cases are shown in Fig. 2. The data was taken at $X/D_0 = 0.2$ downstream of the dump plane. The flame passes through this location for both reacting cases. Swirl has little effect on the passive mean axial profiles (Fig. 2(a)); however, with heat release, the centerline region is strongly effected. Similar trends can be seen in the radial profiles where thermal expansion in the flame normal direction (radially outwards) counters the recirculation effect of the sudden expansion. The peak mean tangential velocity is reduced by heat release compared to Case B.

Root-Mean-Square (RMS) velocity profiles at the same axial location are also plotted in Fig. 3. The swirl effects, while small in the mean, are more profound for the fluctuating quantities. In the shear layer region ($R/D_0 \approx 0.5$), all three simulations show typically high fluctuations. However, the jet core region has distinct differences. As with the mean, the fluctuating axial velocity with heat release is much less. The lower fluctuating velocity in the core shows the stabilizing effect of swirling flows. Little differences are observed in the radial and tangential RMS profiles with or without swirl. Again, heat release is seen to reduce the fluctuating amplitudes.

Shown in Fig. 4 are the pressure fluctuation spectra. The pressure signals were recorded at the base of the dump plane (see Fig. 1) where the vorticity is low. All three simulations reveal a dominant frequency (plus a harmonic) at a Strouhal number (defined as fD_0/U_0) of 0.88 for the cold flow and 1.12 for the hot (with harmonics at 1.76 and 2.24, respectively). Analysis of the pressure amplitudes and phase angles of these pressure signals along the longitudinal axis of the combustor indicated a $3/4$ wave with a wave length proportional to the combustor length (from dump plane to diffuser). This wave shape is acoustic as indicated by the frequency shift from a cold chamber (Case A & B) to hot (Case C), i.e. the frequency shift corresponds to the change in the speed of sound at the higher temperature.

As with the RMS velocity profiles, Fig. 4 gives cre-

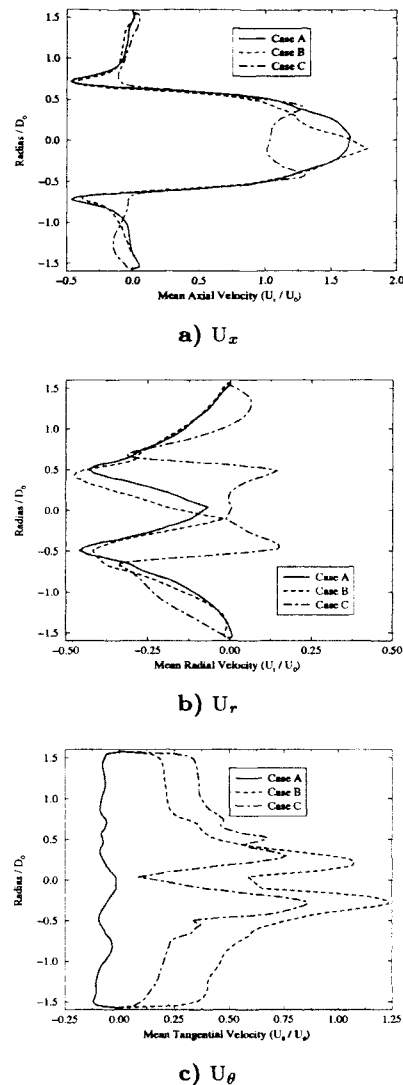


Fig. 2 Mean velocity profiles at $X/D_0 = 0.2$ downstream of the dump plane: (a) axial (U_x), (b) radial (U_r), (c) tangential (U_θ).

dence to the attenuation effects of heat release. While the acoustic wave shape is the same, the amplitude is attenuated by almost 700% when compared to Case B. A time segment of the global Rayleigh parameter ($\bar{R}(t)$)²² (not to scale) is presented in Fig. 5. Positive $\bar{R}(t)$ corresponds to amplification (unstable growth) while negative indicates neutral oscillations or attenuation. This time sequence shows stable operation ($\bar{R}(t)$ is nearly always (-)), i.e. the pressure, p' , and heat release, $\Delta q'$, fluctuations are not in phase. Only at the higher harmonic pressure signal ($St = 2.24$) does amplification occur indicating that the heat release oscillations are at or near the higher frequency.

The mean structure of the flame surface for Case B & C is plotted in Fig. 6. With heat release, the flame surface is pushed outwards (radially). This trend

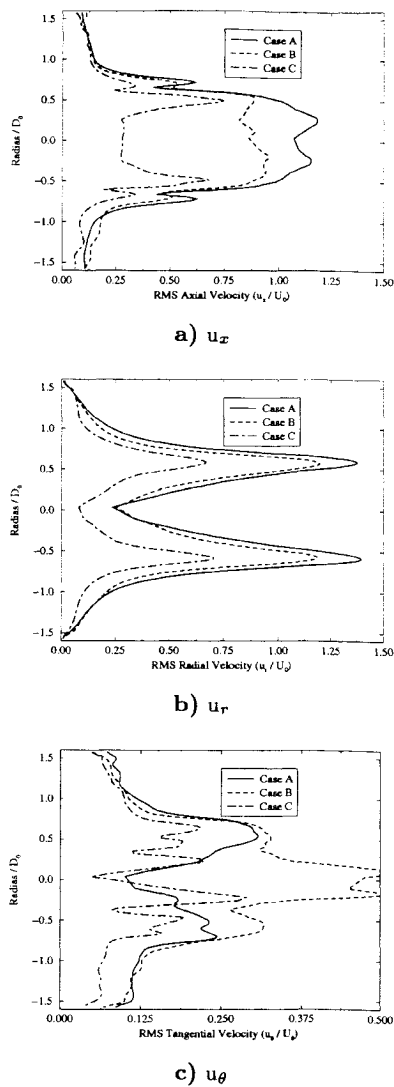


Fig. 3 RMS velocity profiles at $X/D_0 = 0.2$ downstream of the dump plane: (a) axial (u_x), (b) radial (u_r), (c) tangential (u_θ).

follows that of the mean radial velocity profile (Fig. 2(b)) which shows an outward acceleration compared to the zero heat release combustion. The hot flame is longer despite a lower centerline velocity due to a lower turbulence level. This, again, is the effect of turbulence suppression due to heat release.

Fig. 7 shows a mean and an instantaneous view of the 3D flame surfaces for Cases B & C. All pictures were taken with the same frame of references to allow comparison of flame dimensions. Again, with heat release, the flame surface is repelled outward and is longer. Little visual distinction can be made between the cold and hot instantaneous flame fronts. Both show elongation in the azimuthal direction (rib-shaped structures).

The rib-shaped structures in the flame front are

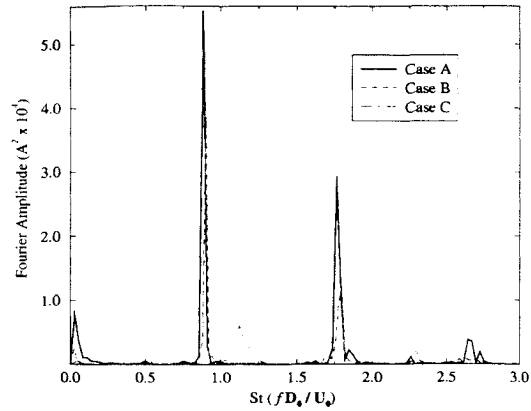


Fig. 4 Fourier transform of pressure fluctuations in the combustor.

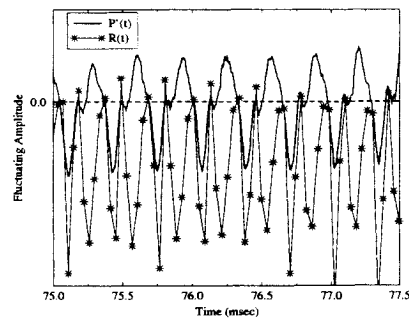


Fig. 5 Time sequence of the volume averaged Rayleigh parameter, $\bar{R}(t)$, showing stable combustion.

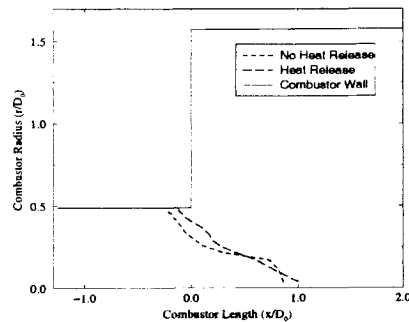


Fig. 6 Mean flame surface location with (Case C) and without (Case B) heat release.

aligned with vortex tubes generated in the swirling boundary in the inlet pipe. An example of these vortex tubes from Case C is shown in Fig. 8. There, axial vorticity, ω_x , is shown in red, vorticity magnitude, $|\omega|$, is gray, and tangential vorticity, ω_θ , is yellow. As the tangential vortices shed, they entrain the flame and carry it along. The flame is drawn outwards till the vortex breaks down. This vortex/flame interaction causes a pulsing flame. More analysis and details of this interaction will be given in future papers.

5 LES of Spray Combustion

Results obtained by solving the unsteady, filtered Navier-Stokes equations for the two-phase reacting flows, with infinite rate chemistry and heat release and a gradient diffusion type of closure for scalars are presented here.

Fig. 9 presents a representative view of the droplet distribution in the combustor for the reacting case. Since the particle size is continuously decreasing due to vaporization, small droplets are entrained into the recirculation bubble due to the swirling motion of the air and are eventually consumed by combustion. On the other hand in the momentum coupled case, (figure not shown) only few particles were seen in the recirculation bubble because of the high inertia of the particles. Large dispersion of droplets towards the outer boundary was also observed in the cross-sectional view (not shown) of the combustor. This radial spread is seen to increase with downstream distance. Larger particles that reach the wall bounce back and move downstream. Further downstream droplets tend to be more uniformly distributed.

Fig. 10 shows the iso-surface of the vorticity and droplet distribution in the combustor. Coherent vorticity is seen near the dump plane is disintegrated quickly in the droplet laden flows. On the other hand, distinct ring structures were observed farther downstream in unladen flows.

Another interesting feature that was observed from the instantaneous snapshots of the flow field is that the droplets tend to accumulate in regions of low vorticity. This type of preferential accumulation of droplets in regions of low vorticity was also observed in the studies of Pannala and Menon.⁴

To investigate this further, conditional expectation of droplet number density conditioned on vorticity is computed. This is shown in Fig. 11. The abscissa in this plot is the normalized vorticity magnitude (normalized by the maximum vorticity in the whole domain). It can be observed that the PDF is non-symmetric, and is biased towards the low-vorticity side, indicating that the droplets tend to accumulate in regions of low vorticity.

Three cases have been simulated to study the effect of particles and combustion on the dynamics of the turbulent flows. A swirling, non-reacting case without droplets, a swirling, non-reacting with droplets with only momentum coupling (i.e., no vaporization) and a swirling, reacting case with droplets and full coupling (with vaporization) were studied. Fig. 12 shows the mean velocity profiles of the gas phase in streamwise, transverse and spanwise directions for all the three cases simulated. These radial profiles are shown at $x/L = 0.1$ (inside the inlet pipe) and 0.14 (slightly downstream of the dump plane). In all these profiles it can be seen that the peak values of the mean velocity have been reduced in the presence of the particles.

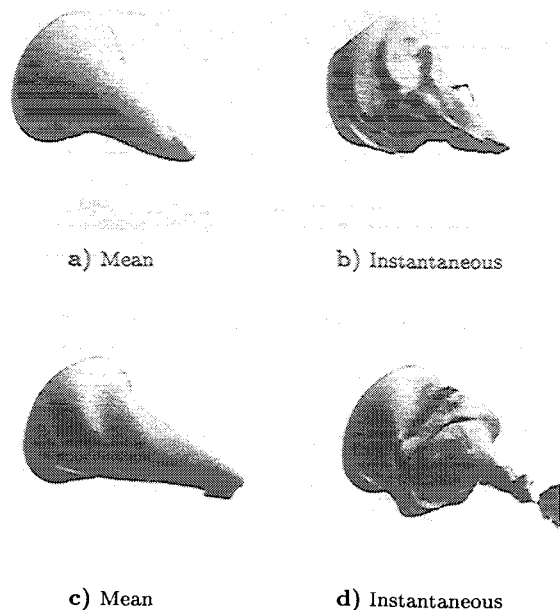


Fig. 7 Mean and instantaneous 3D flame surface: (a) Case B mean, (b) Case B instantaneous, (c) Case C mean, (d) Case C instantaneous. Flow direction is from top left to bottom right.

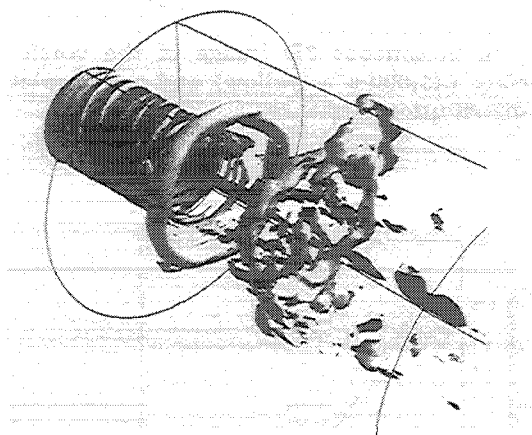


Fig. 8 Vorticity in the combustor: Vorticity Magnitude, $|\omega|$ (gray), Tangential Vorticity, ω_θ (yellow), Axial Vorticity ω_x . Flow direction is from top left to bottom right.

This is the effect of the momentum transfer between the gas phase and the liquid phase. The velocity profiles in the inlet pipe, are almost identical except in the central region of the pipe. This is due to the presence of a greater number of particles near the centerline as compared to near the walls. Both combustion and the droplets seem to have a similar effect on the mean flow, that is to reduce the peak value of the velocities.

Transverse and spanwise mean velocity profiles show that the swirl intensity has been altered significantly in the droplet laden flows. It can be seen that the swirl has been attenuated considerably in the presence of the droplets and combustion. Effect of Stokes number on this attenuation needs to be studied using particles of varying size. It should be noted that for flows with a large droplet to gas-phase density ratio and droplet sizes smaller than the Kolmogorov scale, the particle paths, the relative velocities (between the two phases), and the particle drag are all uniquely determined by the Stokes number.

Fig. 13 shows the root mean square velocity fluctuations in streamwise, transverse and spanwise directions. It can be seen that the turbulent fluctuations have been attenuated in the presence of the particles. The presence of droplets decrease the turbulence level by introducing an additional dissipation. By comparing the magnitude of turbulent intensity profiles in unladen and droplet laden flows, we can see that turbulent fluctuations have been attenuated significantly in regions where the turbulent intensities are high in unladen flows. This is because in regions of high intensities the local Stokes number based on the turbulent time scales will be high. This leads to increased attenuation of the turbulence closer to the shear layer where the turbulence production is very high. This is consistent with Fessler *et al*²³ study in a backward facing step.

Turbulence levels in the recirculating zones are not affected considerably, due to the presence of fewer particles there. Again the presence of fewer particles in the recirculating zone is because of the large Stokes number associated with the particles. As a result, particle inertia is high and hence do not follow the gas phase in the recirculation zone.

6 Conclusions

The results of our LES model development effort subsequent to the progress reported earlier^{24, 25} is summarized in this paper. The past studies established the ability of this solver to carry out accurate Large-Eddy Simulations (LES) using relatively coarse grid resolutions. The algorithm was shown to be capable of capturing unsteady phenomena such as combustion dynamics (premixed), droplet vaporization, and non-premixed spray combustion in practical combustion devices. This approach included a more fundamental treatment of the interaction between the flame

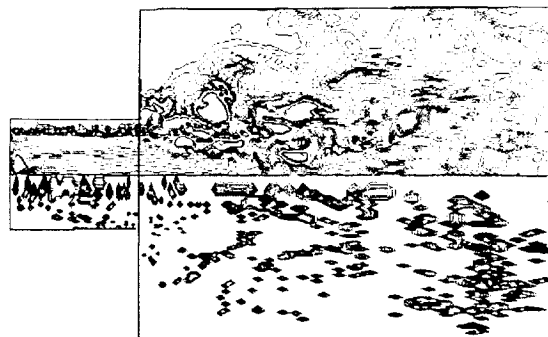


Fig. 9 Cross-plane instantaneous image of the droplet number distribution contours (upper half) and vorticity magnitude contours (lower half).

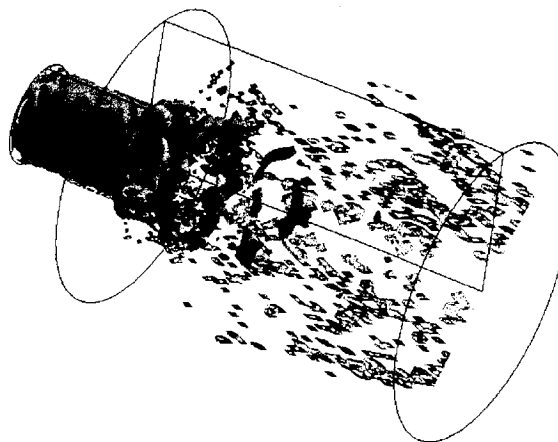


Fig. 10 Instantaneous 3D image of the vorticity isosurface ($45,000 \text{ s}^{-1}$ (yellow)) and the droplet number distribution contours.

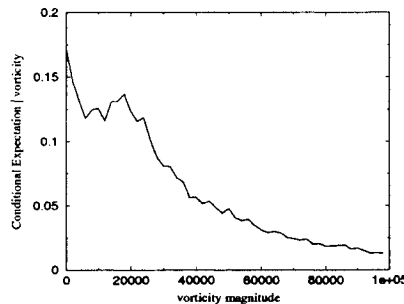


Fig. 11 Conditional expectation of droplet number density conditioned on the vorticity magnitude.

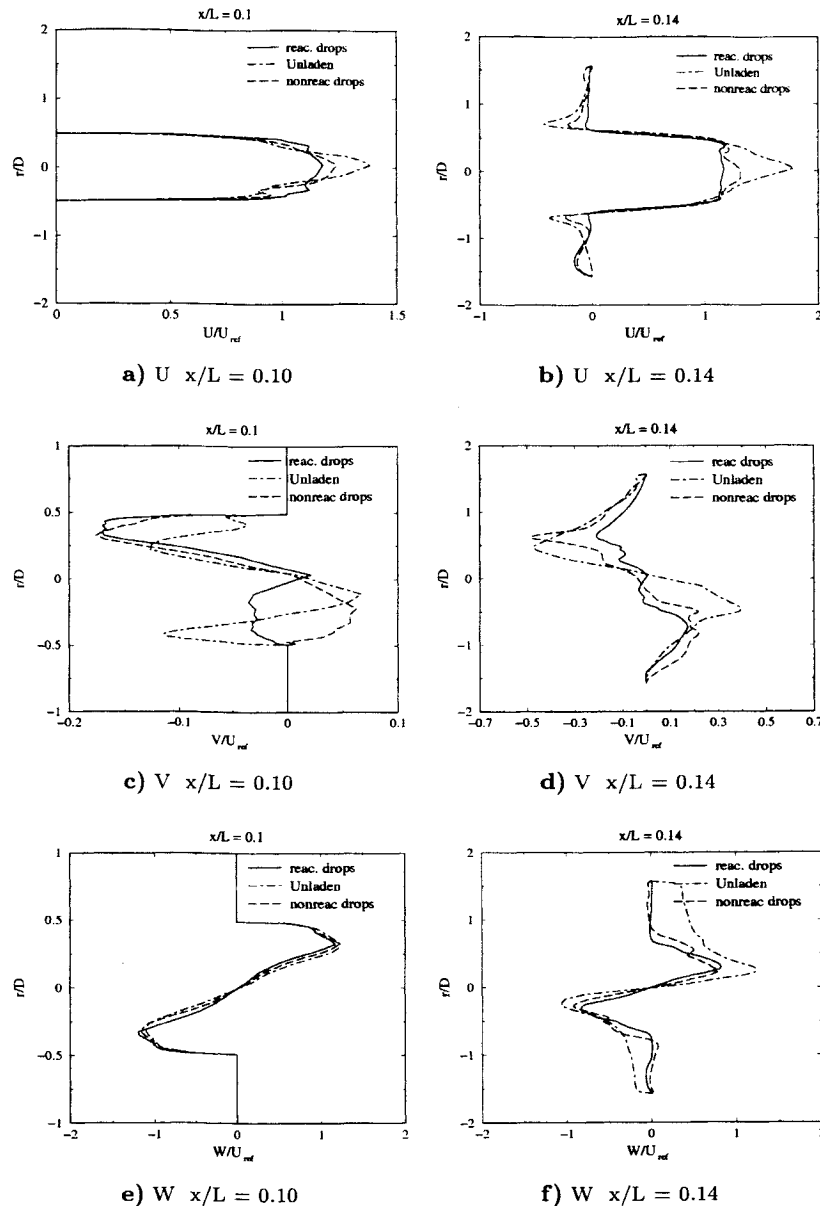


Fig. 12 Mean velocity profiles at two axial locations: (a,b) axial , (c,d) transverse , (e,f) spanwise.

and the flow dynamics while, at the same time, being general enough to allow the inclusion of further complexities of a turbulent combustion encountered in gas turbine combustors. Global behavior of the spray combustion such as the preferential concentration of droplets, droplet dispersion and turbulence modification by the particles are all captured reasonably well by the present formulation. The effects of the mass loading ratio, droplet vaporization rate, and Stokes number on the turbulence modification needs to be studied further. In terms of model development, efforts are underway to include droplet-droplet interaction and a void-fraction approach to simulate the final stages of droplet evaporation. Implementation of the Linear

Eddy Model (LEM) for the scalar transport closure with finite rate chemistry is also currently in progress.

7 Acknowledgments

This work was supported in part by the Army Research Office (ARO) under the Multidisciplinary University Research Initiative (MURI) and General Electric Power Systems. Computational time was provided by DOD High Performance Computing Centers at NAVO (MS), SMDC (AL), WPAFB (OH), and ERDC (MS) under ARO and WPAFB HPC Grand Challenge Projects.

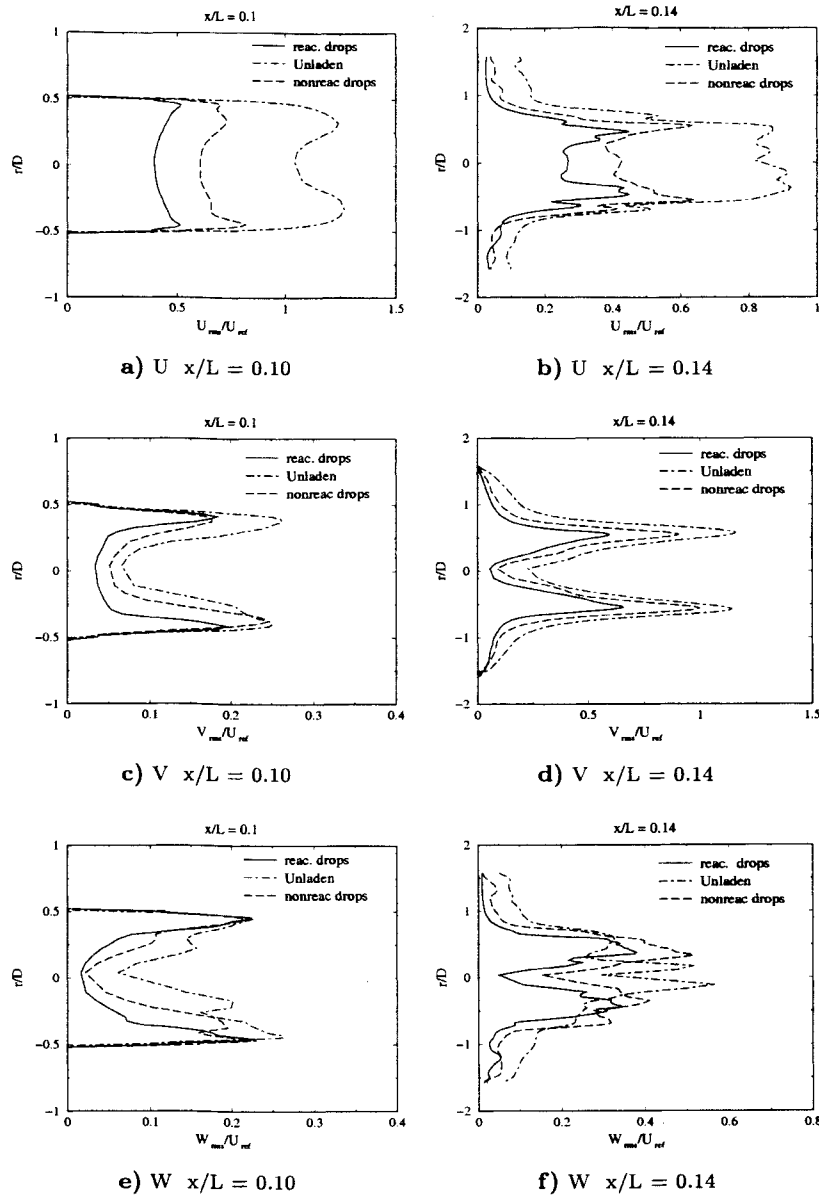


Fig. 13 Mean velocity profiles at two axial locations: (a,b) axial (c,d) transverse (e,f) spanwise.

References

- ¹ Kim, W.-W., Menon, S., and Mongia, H. C., "Large Eddy Simulations of a Gas Turbine Combustor Flow," *Combustion Science and Technology*, Vol. 143, 1999, pp. 25–62.
- ² Kim, W.-W. and Menon, S., "Numerical Modeling of Turbulent Premixed Flames in the Thin-Reaction-Zones Regime," *Combustion Science and Technology*, Vol. 160, 2000, pp. 1–32.
- ³ Chakravarthy, V. and Menon, S., "Large-Eddy simulations of turbulent premixed flames in the flamelet regime," *Combustion Science and Technology*, Vol. 162, 2001, pp. 1–48, to appear.
- ⁴ Pannala, S. and Menon, S., "Large eddy simulations of two-phase turbulent flows," *AIAA 98-0163, 36th AIAA Aerospace Sciences Meeting*, 1998.
- ⁵ Erlebacher, G., Hussaini, M. Y., Speziale, C. G., and Zang, T. A., "Toward the Large-Eddy Simulation of Compressible Turbulent Flows," *Journal of Fluid Mechanics*, Vol. 238, 1992, pp. 155–185.
- ⁶ Menon, S., Yeung, P.-K., and Kim, W.-W., "Effect of Subgrid Models on the Computed Interscale Energy Transfer in Isotropic Turbulence," *Computers and Fluids*, Vol. 25, No. 2, 1996, pp. 165–180.

- ⁷ Kim, W.-W., *A New Dynamic Subgrid-Scale Model for Large-Eddy Simulation of Turbulent Flows*, Ph.D. thesis, Georgia Institute of Technology, Atlanta, GA, September 1996.
- ⁸ Yakhot, V., "Propagation Velocity of Premixed Turbulent Flames," *Combustion Science and Technology*, Vol. 60, 1988, pp. 191-214.
- ⁹ Menon, S., McMurtry, P., and Kerstein, A. R., "A Linear Eddy Mixing Model for Large Eddy Simulation of Turbulent Combustion," *LES of Complex Engineering and Geophysical Flows*, edited by B. Galperin and S. Orszag, Cambridge University Press, 1993.
- ¹⁰ Smith, T. M. and Menon, S., "Subgrid Combustion Modeling for Premixed Turbulent Reacting Flows," *AIAA-98-0242*, 1998.
- ¹¹ Chakravarthy, V. and Menon, S., "Subgrid Modeling of Premixed Flames in the Flamelet Regime," Flow, Turbulence and Combustion (submitted).
- ¹² Oefelein, J. C. and Yang, V., "Analysis of trans-critical spray phenomena in turbulent mixing layers," *AIAA 96-0085, 34th AIAA Aerospace Sciences Meeting*, 1996.
- ¹³ MacCormack, R. W., "The effects of viscosity in hyper-velocity impact cratering," *AIAA Paper 69-354*, 1969.
- ¹⁴ Nelson, C. C., *Simulations of spatially evolving compressible turbulence using a local dynamic sub-grid model*, Ph.D. thesis, Georgia Institute of Technology, Atlanta, GA, December 1997.
- ¹⁵ Poinso, T. and Lele, S., "Boundary Conditions for Direct Simulations of Compressible Viscous Flow," *Journal of Computational Physics*, Vol. 101, 1992, pp. 104-129.
- ¹⁶ Zinn, B. and Neumeier, Y., "Control of combustion instabilities with secondary fuel injection using real time modes observation: practical implementation," *Proceedings of the 26th International Symposium on Combustion*, 1996.
- ¹⁷ Pashereit, C. O., Gutmark, E., and Wolfgang Weisenstein, W., "Control of thermoacoustic instabilities and emissions in an industrial-type gas-turbine combustor," *Proceedings of the 27th International Symposium on Combustion*, 1998, pp. 1817-1824.
- ¹⁸ Paschereit, C., Gutmark, E., and Weisenstein, W., "Coherent structures in swirling flows and their role in acoustic combustion control," *Physics of Fluids*, Vol. 11, No. 9, 1999, pp. 2667-2678.
- ¹⁹ Sivasegaram, S. and Whitelaw, J., "The influence of swirl on oscillations in ducted premixed flames," *Combustion Science and Technology*, Vol. 85, 1991.
- ²⁰ Smith, T. M. and Menon, S., "The Structure of Premixed Flames in a Spatially Evolving Turbulent Flow," *Combustion Science and Technology*, Vol. 119, No. 1-6, 1996, pp. 77-106.
- ²¹ Pocheau, A., "Scale invariance in turbulent front propagation," *Physical Review E*, Vol. 49, 1994, pp. 1109-1122.
- ²² Menon, S., "Active combustion control in a ramjet using large-eddy simulations," *Combustion Science and Technology*, Vol. 84, 1992, pp. 51-79.
- ²³ Fessler, J. R. and K., E. J., "Turbulence modification by particles in a backward facing step flow," *Journal of Fluid Mechanics*, Vol. 394, 1999, pp. 97-117.
- ²⁴ Menon, S., Kim, W.-W., Chakravarthy, V. K., Pannala, S., and Henry, W., "Parallel Simulations of Turbulent Reacting Sprays," *AIAA-99-3438*, 1999.
- ²⁵ Menon, S., Kim, W.-W., Stone, C., and Sekar, B., "Large-Eddy Simulation of Fuel-Air Mixing and Chemical Reactions in Swirling Flow Combustor," *AIAA-99-3440*, 1999.